QUASI-STATIC AND DYNAMIC CRUSH BEHAVIOUR OF 3D PRINTED THIN-WALLED PROFILES REINFORCED WITH CONTINUOUS CARBON AND GLASS FIBRES

U. Morales (*), A. Esnaola, M. Iragi, L. Aretxabaleta and J. Aurrekoetxea

Mechanical and Industrial Production Department,
Mondragon Unibertsitatea, Loramendi 4, 20500 Mondragón, Spain
Corresponding Author (*) Email: umorales@mondragon.edu, Web Page: http://www. mondragon.edu

Abstract

The present study analyses the quasi-static and dynamic crush behaviour of 3D printed thin-walled hollow profiles reinforced with continuous carbon (cCF/PA) and glass fibres (cGF/PA), in axial and radial loading. Despite the specific microstrutural differences generated during 3D printing, the nature of the constituents (fibre and matrix) controlled the differences between the crush behaviour of both profiles. Although a stable collapse mode was observed for each profile under quasi-static and impact loading, a ductile response was only reported for the cGF/PA profiles. Under radial quasi-static conditions the cCF/PA profiles showed *SEA* values greater than the cGF/PAs. Nevertheless, the radial impact performance of the cGF/PA profile was greater as the material presented a strain-rate dependency. The obtained radial *SEA* values obtained for steered glass fibres were at least four times higher than the best values found in the literature. Thus, concentrically printed cGF/PA reinforcements could be exploited for impact loaded hollow profiles applications.

Keywords: E. 3D printing, B. Impact behaviour, B. Microstructures, A. Polymer-matrix composites.

1. Introduction

Sustainable design is presently a driving force in automative component development, with lightweight design, energy saving, and efficient use of raw materials becoming the subject of much research. However, in parallel with environmental concerns, safety remains a critical factor, and manufacturers must strive to ensure or improve passenger safety in crash situations [1,2].

In this context, fibre reinforced polymers (FRP) have gained traction in the automotive industry due to their lightweight properties, specific strength and stiffness, corrosion resistance, cost and ease of manufacturing [3]. One further advantage is that the energy absorption mechanisms of these composite structures are based on progressive material collapse in a brittle manner, as opposed to metallic structures which are designed to absorb energy by plastic deformation [4]. From the design point of view, most crashworthiness components are

conceived as thin-walled spaceframes, since these profiles are able to dissipate high levels of energy in impact scenarios [5-6]. Several authors [4-13] have reported that the main parameters affecting specific energy absorption (*SEA*) of composite structures are the profile transverse section, the design and location of triggers, the reinforcement architecture, the fibre orientation, and the fibre and void contents. Most studies found in the literature concerning automotive structures design are focussed on continuous fibre reinforced thermosetting polymers (cFRP) with non-complex cross sections manufactured by conventional processes [7-9]. However, continuous fibre reinforced thermoplastics (cFRTP) are replacing conventional thermosetting composites due to their shorter process cycle time, recycling rate and *SEA* for impact loading structural components [14]. Nevertheless, the drawbacks of cFRTP manufacturing processes are similar to those of cFRP.

Additive manufacturing, and namely continuous Fibre Fabrication (cFF), allows the use of thermoplastic materials in combination with complex geometries, or steered fibre orientations, to satisfy the demand for new lightweight design concepts in the transportation industry [15-17]. Of the current cFF approaches, the highest mechanical properties and fewest impregnation and compaction problems are achieved with cFRTP pre-impregnated printing technologies [18]. This approach has been successfully applied to polyamide matrix (PA) reinforced with continuous Carbon (cCF/PA), Glass (cGF/PA) and Kevlar©(cKF/PA) fibres using cFF techniques [19-21].

The characterisation of the mechanical properties of printed cCF/PA and cGF/PA have been carried out by several authors following standard testing methods such as tensile [19-22,24,28-30], compression [24,26-28], bending [19,23,27,29], in-plane shear [24,26,28], out-of-plane shear [26], interlaminar strength [23,25,28], quasi-static indentation [23] and interlaminar fracture (Mode I and Mode II) [28]. Three main conclusions can be drawn from these quasi-static studies:

(i) similar failure behaviour in cCF/PA and cGF/PA were reported under tension, but differences were observed in the compression behaviour,

(ii) according to the ILSS (interlaminar shear strength) tests, different adherence of layers was shown to lead to different fracture patterns, crack growth and hence energy absorption capability of printed cCF/PA and cGF/PA composite materials and,

(iii) the highest values of tensile strength and stiffness were reported for cCF/PA specimens.

However, no studies investigating the complex geometry, or the dynamic crushing of printed cCF/PA and cGF/PA profiles have been found. Only one paper concerning impact loading (Charpy impact test) of printed

cCF/PA and cGF/PA was identified, in which cGF/PA samples exhibited the highest impact strength, and cCF/PA samples the lowest [32]. The lack of wettability of glass fibre bundles by the PA was found the main factor, which causes extensive delamination, reduces ILSS but improves the impact resistance of printed cGF/PA [25]. As regards the matrix of printed cCF/PA and cGF/PA composites, Pascual-González *et al.* [31] studied the composition and microstructure of pre-extruded cCF/PA and cGF/PA filaments. Differences in the thermal properties (DSC, TMA) of PA matrix were found which could explain the variations on their mechanical performance [23,25,26,32]. Moreover, the printed amorphous structure of cCF/PA and the semicrystalline structure of cGF/PA showed a different glass transition temperature (T_g), 143 and 50 ºC, respectively. Since a significant variation on the structure and T_g were found [31], a different impact response and strain-rate sensitivity is envisaged.

Furthermore, a search of the literature has revealed a considerable body of work concerning the impact behaviour of conventional cFRP and cFRTP profiles [6,13,33,34], however the strengthening of 3D printed cCF/PA and cGF/PA profiles due to the crush test speed remains unstudied. Enhanced energy absorption capability of a glass fibre reinforced polymer (GFRP) profile was reported and related to a strain-rate dependency [33]. In addition, Farley *et al.* [34,35] showed that the strain-rate effect on energy absorption capability increases as the fibre orientation differes from 0º. Increasing the fibre orientation angle promotes the interlaminar failure and plastic deformation of the matrix and consequently higher energy absorption can be dissipated in a stable failure mode [36,37]. The viscoelastic nature of the matrix also influences the behaviour of the composite, since from one side there is a strain-hardening phenomenom, but there is an opposite effect induced by the adiabatic heating at high strain-rates [38]. Regarding the strain-rate influence on the fibre behaviour, Arao *et al.* [39] found that carbon fibres are insensitive to the test speed due to their low fracture toughness, whereas glass fibres display certain influence from the test speed due to their slower crack growth.

The present study analyses the quasi-static and dynamic crush behaviour of 3D printed thin-walled hollow profiles of polyamide composites reinforced with continuous carbon and glass fibres. To this end, two reinforcement materials (carbon and glass), two compression test speeds (static and dynamic), as well as two loading directions (axial and radial) were analysed. The objective of this study therefore, is to characterise the impact behaviour and specific energy absorption (*SEA*) capability of the profiles. The collapse mode and fracture micro-mechanisms were also investigated, to understand the influence of the reinforcement material and strain-rate.

2. Experimental procedures

2.1. Materials

Test specimens were produced using a Mark Two® 3D printer from Markforged. The printed composite materials employed were a continuous carbon fibre reinforced polyamide (cCF/PA) and a high strength high temperature fibreglass reinforced polyamide (cGF/PA). A polyamide 6 reinforced with carbon micro-fibres (Onyx®) was used as the infill material.

2.2. Specimen design and the 3D printing process

The transverse section of the profile is shown in Figure 1, and its geometrical properties are summarized in Table 1. The Fold (Figure 1) was based on the transverse sections with radial corrugation studied by Belingardi *et al*. [10]. The quasi-static compression and impact test specimens were 60 mm in length with 3 mm thickness profiles. The sample mass was 24 g for cCF/PA and 30 g for cGF/PA.

{Insert Figure 1}

{Insert Table 1}

The cCF/PA and cGF/PA profiles were printed following a concentric printing strategy for continuous fibre placement with the x-axis perpendicular to the bed. In the concentric approach, the printing head follows the outer profile of the part and places a single strand of fibre inwards in rings from that outer boundary. The starting point is a potential area of weakness, so in each layer Eiger® (slicer software from Markforged) automatically moves this starting point around the part, generating a good overlap. For all the specimens, the filling density was 100% and only one contour wall of Onyx® was used to maximize the fibre content. The extrusion and filling parameters used to print the specimens are shown in Table 2. In MarkTwo® 3D printer processing parameters, such as layer thickness and interbead spacing are predefined by Eiger© and therefore the pressure applied is not controlled. Before testing, the specimens were conditioned for 48 hours at 23 ºC and 55% RH.

{Insert Table 2}

The name codification of the specimens is as follows; the first capital letter refers to the fibre reinforcing material of the profile (C for carbon and G for Glass), the second identifies the compression test velocity (S for Static and D for Dynamic), and the third identifies the loading direction (A for Axial and R for Radial).

2.3. Microstructure and fracture surface inspection

The microstructure, fibre distribution and voids of the printed specimen were characterized using an optical microscope (OLYMPUS-GX51). The samples have been prepared by the following procedure: the samples were cut perpendicular (transverse view) or parallel (longitudinal view) to the xy-plane, ground using 600 grit SiC paper, and then polished with a 1 µm monocrystalline diamond suspension applied to a polishing cloth. Failure modes were studied by analysing the fracture zones of the printed profile with an optical microscope (Leica DMS 1000).

2.4. Crush tests

Quasi-static compression tests were carried out using a Hoyton/HM-D universal testing machine equipped with a 100 kN load cell. The overall displacement was registered from the encoder of the ball-screw. The crosshead speed was 10 mm/min along the collapse distance *l*, and the tests were carried out at room temperature and 55% RH.

Impact tests were performed using a Dynatup 8120 drop-weight test machine with a mass of 144.5 kg. A drop height of 0.5 m and a flat-ended tip impactor was used. The velocity of the impact test was measured by the photocell (3,2 m/s). The test machine is equipped with a 200 kN load cell to record the load-time response and the tests were carried out at room temperature and 55% RH. Displacement-time and energy-time data were also calculated.

The specific energy absorption *SEA* (kJ/kg); mean load P_{mean} (kN), maximum load P_{max} (kN) and load crush force efficiency *CFE* (-), were calculated from the registered force-displacement curves by the following equations:

$$SEA = \frac{\int_0^{l_{\max}} P(l)dl}{m_{\text{t}}} \tag{1}$$

$$P_{\text{mean}} = \frac{\int_0^{l_{\max}} P(l)dl}{l_{\max}} \tag{2}$$

$$CFE = \frac{P_{mean}}{P_{max}} \quad (3)$$

where, l_{max} (mm) is the total collapsed length and m_t is the crushed specimen mass (kg). The total collapsed length corresponds to 60% of the total height of the specimen. Nevertheless, the static compression tests were conducted until material densification or separation, which is the moment when a significant profile stiffness change or exponential increase of the load curve occurs. A minimum of three samples were tested for each material-test combination.

3. Results and discussion

3.1. Microstructure analysis

The 3D-printing process generated similar microstructure and defects in both materials. The optical microscope images at different magnification of the cross section and longitudinal section of concentric printed cCF/PA and cGF/PA samples are shown in Figure 2. The non-homogeneous fibre bundles distribution and resin-rich zones can be observed for both materials and have their origin in the initial filament microstructure, as reported by Goh *et al.* [23]. Furthermore, no voids were observed into the bead at the observation magnification scale.

As regards the interlayer bonding quality, printing tracks were visible (Figure 2a and 2b) and a high concentration of voids were observed close in the interlayer zone (Figure 2c and 2d). The thickness and width of the different layers were regular. Similar bead widths (1 mm) occur, even if the initial diameters of cCF/PA and cGF/PA are different, in this case 380 and 340 µm respectively, since both filaments were flattened by a factor of three during the printing process [20,23].

The interface between the adjacent beads was also identifiable due to the presence of large voids. Since the overlap between beads was not uniform along the printing path, the longitudinal interbead voids were visible (Figure 2e and 2f), as previously reported by Goh *et al*. [23]. These voids were also visible in the transversal section of the sample (Fig. 2c and 2d).

Even when the printing path was straight, the layered beads presented undulations (Figure 2g and 2h), generating the aforementioned interbead voids [30]. The effect of fibre waviness was more marked in the cGF/PA case due to its lower stiffness, as reported by Chabaud *et al.*[20].

In the interface between the Onyx wall contour and the inner fibre reinforced beads, significant differences between the two materials were found. In the case of the cCF/PA some voids were generated but there was sufficient overlap to ensure contact between the materials (Figure 2i), whereas in the cGF/PA the lack of overlapping in some layers generated large voids (Figure 2j).

{Insert Figure 2}

Color should be used for Figure 2 in print

3.2. Fibre placement analysis

The influence of profile geometry, prepeg filament stiffness and the printing pattern on fibre-placement defects at critical locations such as corners, radii and edges of the profiles are analysed in this section. These critical points are of special interest, since they correspond to stress concentration areas for crack and failure initiation, and thus the presence of defects in these locations can increase the risk of premature failure of the structure [40]. Defects on cCF/PA samples are shown in Figures 3a-c and cGF/PA in Figures 3d-f. It is important to note that a concentric printing pattern follows a spiral path starting at the outside contour and finishes inward [30]. This motion induces fibres undulations [41,42], and generates interbead voids as can be observed in Figure 3a and 3d. For radii larger than 3 mm fibre twisting (Figure 3b and Figure 3e) was observed, which is related to the restricted rotation of the extrusion head during a curved path [20, 41,42]. Evidences of fibre twisting and folding back were observed in zones with radii from 1 to 3 mm in the two materials (Figure 3b and Figure 3e). The folding back caused a local fibre breakage in the cCF/PA beads (Figure 3c), whereas no fibre breakage was observed for cGF/PA (Figure 3f).

{Insert Figure 3}

Color should be used for Figure 3 in print

3.3. Quasi-static compression test

3.3.1. Axial crushing pattern

The axial crushing patterns of the two materials are shown in Figure 4. The crush behaviour of FRP profiles during axial compresion are classified as progressive (stable) or catastrophic (unstable) [4]. The general axial crushing behaviour of the FRP profiles can be divided in two stages: the first stage is driven by the elastic

response of the material, whereas the second stage is governed by the material plasticity and fracture toughness. The crushing curves and failure modes of both materials presented common features at the first stage: an initial elastic zone (1) until the first peak load is reached (2), then crushing collapse begins and load drops (3). The crushing curves for the samples with catastrophic failure finish at this point, whereas those with progressive collapse continues under a constant load (4). Finally, the densification of the sample due to section folding induces the load to rise (5). Figure 4 also shows representative pictures of the samples in each of the crushing stages.

The crushing pattern of the CSA and GSA samples both exhibited a stable crushing mode driven by a pseudo-ductile (2) failure mechanism of progressive folding. A large plateau stage (4), followed by a secondary peak load (5), was observed which might be due to material densification when section buckled. The CSA specimen however, presented the longest crushing length load whereas the GSA showed the highest peak load. Furthermore, the amount of energy absorbed by the GSA was higher than the CSA. The presence of concentrically oriented continuous fibres influenced directly the failure mechanism, and therefore the energy absorption capability of the printed profiles. The fibre rings not only prevented longitudinal crack generation but also promote a collapse mechanism based on a local barrelling of the profile followed by a local buckle, and subsequent progressive axial folding. As can be seen in the *SEA* values set out in Table 3, both profiles exhibited enhanced energy absorption properties with similar *SEA* values. In fact, the highest *SEA* value (31.4 kJ/kg) corresponding to the GSA sample and was 4% more than the CSA sample. On the other hand, the CSA showed the lowest peak load value (22.2 kN) which is favourable from the crushing point of view. In addition, the mean load value reached for the GSA (15.7 kN) was higher than the corresponding mean load for the CSA (12.0 kN), which means a higher *CFE* of 63% for the GSA sample.

{Insert Figure 4}

Color should be used for Figure 4 in print

3.3.2. Radial crushing pattern

The radial crushing behaviours of the two materials are shown in Figure 5. Their typical radial progressive crushing patterns are divided in three stages; the first stage is driven by linear elasticity (1) until the first hinges are generated in critical points of the transverse section (2), such as corners, thickness changes or corrugations. These points have been identified by other authors as stress concentration zones and crack tips initiators for

progressive tearing lines in the longitudinal direction [10]. In the second stage, the crushing mechanism continues and the transverse section geometry undergo significant changes (3), developing larger deformed zones at the critical points. In the final stage, the load increases gradually as the amount of collapse hinges increases (4) and the inner walls of the sections make contact (5 and 6).

The materials of both samples (CSR and GSR) exhibited a pseudo-ductile response, with a spring-back effect during the unloading path, being more evident in the GSR profile. No sharp peaks were observed during the hinges formation of the GSR, whereas the CSR sudden load drop denotes breakage of the carbon fibre rings. Higher loads were reached, and higher energy was also absorbed during the CSR crushing, since the CSR corners were reinforced by continuous carbon fibres. Despite the fact that the response of the GSR profile was slightly lower than the CSR, the load level at plateau stage was higher.

Turning to the *SEA* values set out in Table 3, the highest values were obtained for the CSR sample. The cCF/PA reinforcement material, and namely CSR, delivered the best energy absorption performance under radial loading with a *SEA* value of 9.0 kJ/kg, whereas GSR absorbed 6.9 kJ/kg. Moreover the CSR sample exhibited the highest maximum load and radial stiffness, reaching a maximum load of 15.4 kN.

{Insert Figure 5}

Color should be used for Figure 5 in print

{Insert Table 3}

Similarities were found between the collapse curves of samples with cCF/PA and cGF/PA samples, since both materials allowed the formation of hinge-like areas at the transverse section corners, driving the progressive failure of the profiles. These hinge-like formations (location and sequence) and their progress were identified as a trigger of stable collapse during the crushing process. Although carbon fibre breakage occurred during hinges formation, this local failure did not affect the global structure integrity and was able to withstand the load during the crushing process. It can therefore be concluded that the reinforcement material does not influence the crushing behaviour of the profiles. Furthermore, a more ductile behaviour of cGF/PA profile was observed due to higher flexibility and toughness at the corners of the profile section.

The cCF/PA material exhibited the best *SEA* values, 30.1 kJ/kg in axial and 9.0 kJ/kg in radial loading. A softer response of the GSA samples was expected since the higher elasticity of the cGF/PA filament allows the profile to fold without fibre breakage and elastic spring-back. Furthermore, a lower peak value (10.4 kN) was recorded for the GSR profile response, which means a lower severity in radial collapse.

3.3.3. Fracture surface inspection

The failure patterns described in the previous sections were completed with the analysis of the fracture micromechanism at the failure points (see Figure 6).

- *Axial static test.*

Fibre splaying and fibre breakage failure mechanisms were observed during folding for the CSA profile, promoting finite fibre debonding and slippage to absorb the energy. Evidence of fibre pull-out during carbon fibre ring expansion was found (Figure 6a), which might be a result of the aforementioned matrix-fibre failure [23,28]. Furthermore, the GSA profile did not show signs of fibre splaying or fibre breakage since a smaller folding radii was allowed by the cGF/PA profile (Figure 6b). The energy absorption mechanism was therefore mainly due to material plasticity and layer and fibre debonding. Therefore, the amount of void or defects, found in layer interface or interbead, allowed a stable collapse and enabled a progressive energy absorption.
The absence of fibre breakage could explain elastic restitution of GSA. In addition, there were noticeable signs of fibre bridging in GSA sample, located mainly between folds, which supports the hypothesis that fibre impregnation was quite fair.

- *Radial static test.*

The formation of hinges allowed stable crushing of the profile for the CSA and GSA profiles. Evidence of the fracture mechanism based on interlaminar shear failure was observed in the post-buckled profiles. Interlaminar failure occurred at interbead level of both printed materials, since large voids were found in printed samples. Interbead friction contributed to a slow crack-growth mechanism, which allowed continuous absorption of energy without affecting the stability of the profile (Figure 6c and 6d). Additionally, transversal cracks of the fibres only appeared at the radii of the CSR postbuckled profile (Figure 6c), whereas the GSR profile shown fibre re-aligment and debonding from the Onyx© wall contour (Figure 6d). These transversal crack tips of the CSR fibres have been caused by carbon fibre folding back and consequence breakage during the printing process.

{Insert Figure 6}

Color should be used for Figure 6 in print

3.4. Dynamic compression test

3.4.1. Axial impact pattern

The axial impact behaviours of the two materials profiles are shown in Figure 7. A collapse mode of folding and stable collapse was observed, as in the quasi-static tests, for CDA and GDA specimens. In both cases, the peak loads reached for dynamic test were lower than those of the static test. The CDA dynamic response curve presented sharp peak loads due to brittle carbon fibre failure, whereas the GDA exhibited a rounded peak load in accordance with the ductile behaviour of the glass fibre. The GCA profile displayed a strain-hardening effect after first peak load was reached, in contrast to the CDA sample which suffered a sudden load drop to almost zero. In contrast to the GDA specimen behaviour, no springback phenomenon was observed for the CDA specimen as a result of the amount of fibre breakage.

The highest *SEA* value was reached for the GDA sample (20.1 kJ/kg), which represented 64% of the quasi-static *SEA* value, as shown in Table 4. In addition, CDA samples also showed a significant descrease of *SEA*, reaching only the 54% of the quasi-static *SEA* value. The *CFE* achieved by the CDA (33%) and GDA specimen (52%) were lower than those of the quasi-static test.

3.4.2. Radial impact pattern

Figure 8 shows, the radial impact behaviours of the CDR and GDR samples and a stable radial collapse mechanism can be seen in both. As was the case with to the radial crushing, the impact collapse was driven by hinges formation at critical point of the geometry. The radial impact load curve of GDR sample was higher than that of the CDR, reaching a higher load level for a shorter collapse distance. Moreover, the post-impacted GDR profile presented a residual stiffness whereas the CDR was completely bent.

The highest *SEA* values (12.8 kJ/kg) were obtained for the GDR profile, whereas the CDR absorbed 4.4 kJ/kg, as shown in Table 4. Moreover the GDR sample exhibited the highest maximum load, reaching a maximum load of 19.0 kN, comparable to the GDA, with a *CFE* of 58%. In contrast, the CDR profile only achived a peak load of 7.4 kN with a *CFE* of 40%. A strengthening effect was observed in the GDR samples due to the increase of crushing speed and thus, GDR could withstand higher loads and absorb more energy before collapse. Therefore, the cGF/PA energy absorption capability was improved, about 85%.

{Insert Figure 8}

Color should be used for Figure 8 in print

{Insert Table 4}

The cGF/PA material exhibited the best *SEA* values with 20.0 kJ/kg and 12.8 kJ/kg, in axial and radial loading respectively. As the cGF/PA material presented a strain-rate dependency, its dynamic performance was enhanced whereas the cCF/PA exhibited a marked reduction of mechanical properties. Moreover, the strain-rate dependency could explain the higher volume of broken fibres reported in the post-impacted cGF/PA samples, in case of axial impact loading. No residual stiffness was observed in the post-impacted the cCF/PA samples due to a lower fracture toughness. In contrast, the cGF/PA samples presented an elastic restitution and residual strength after impact. This demonstrates that the cGF/PA profiles were able to absorb a secondary impact and thus preserved structural integrity during crash events better than the cCF/PA. These results are in good agreement with the study of Arao *et al.* [39], where a strain-rate dependency of glass fibres was related to slower crack growth comparing to carbon fibres. The present study also found that, the radial impact behaviour of concentrically oriented cGF/PA and cCF/PA profile was highly dependent on the PA matrix and thus, interlaminar failure mechanisms that involve matrix shear fracture were observed along interlayer and interbead. The energy absorption modes related to interlaminar failure indicated matrix plastic deformation, fracture and slippage.

3.4.3. Fracture surface inspection

The post-impacted profile were analysed and the following fracture micromechanism at the failure points were reported (see Figure 9)

- *Axial impact test.*

As with the quasi-static test, the main fracture mechanisms of the impacted CSA profile were fibre splaying and fibre breaking (Figure 9a). While the impact energy level absorbed by the CDA sample was lower, the amount of fibre ring breaking was greater than in the quasi-static case. Fibre breaking was also reported in the post-impacted GDA profiles (Figure 9b) however, there was no sign of fibre splaying signs. Moreover, the variation on the fracture mechanism of GDA could explain the decrease of the axial *SEA* value, since energy absorption was controlled by the glass fibre breakage mechanism. Furthermore, evidence of fibre pull-out was observed in the crushed specimens of both materials.

- *Radial impact test.*

Although both specimens presented a stable collapse under radial impact, the CDR exhibited brittle folding, whereas a ductile response was observed for GDR profile. Longitudinal cracks and fibre breakage are shown in Figure 9c y 9e), and might be due to the lower toughness and elongation until breakage of cCF/PA. In contrast, interbead and interlayer crack can be seen in Figure 9d and 9f. Differences in the hinge-like formations were also found when comparing the fracture surface of both materials. While, the lamina bending and debonding mechanism gave rise to the plastic hinge formation in the GDR samples, the transverse tensile fracture mechanism provoked the brittle breakage CDR fibre rings. Therefore, no variation of the fracture mechanism was observed in both materials.

{Insert Figure 9}

Color should be used for Figure 9 in print

From the results of the present study it can be concluded that the nature of the constituents (fibre and matrix) controlled the differences between the crush behaviour of both profiles, rather than the specific microstrutural differences generated during 3D printing. In fact, the amorphous nature of the cCF/PA matrix and the semicrystalline of the cGF/PA [31] could explain the difference between the fracture mechanisms and the strain-rate dependency exhibited by the cGF/PA samples. Firstly, the bonding between layers and beads were different in both materials; the lower interface performance of the cGF/PA samples promoted the stable growth in the delaminated zone [25] and enhanced the slippage between layers instead of fibre breakage, as shown in Figure 9.

Regarding the strain-rate effect, the heat transfer conditions must be considered. At low strain rates the heat generated during crushing could be evacuated and thus the temperature does not change. However, during the impact tests, there was less time to evacuate the heat and the sample temperature rose [38]. Consequently, since the glass transition temperature of the cGF/PA matrix is around 50 ºC, and the cCF/PA matrix is close to 150 ºC [31], the higher softening of cGF/PA enables higher energy dissipation. Additionally, the glass fibres showed strain-hardening behaviour, as in the case of [39], whereas the carbon fibres did not, allowing better performance under impact loadings.

4. Conclusions

The present study has analysed the quasi-static and dynamic crush behaviour of 3D printed thin-walled profiles reinforced with continuous carbon and glass fibres. The 3D-printing process generated similar microstructure and defects in both materials, and the most significant microstructural aspect was the steered fibre orientation. Since the samples were printed using a concentric fibre printing pattern, fibre twisting and folding back were found for radii smaller than 3 mm, but above this size only fibre twisting appeared. Waviness of the fibre bundles were observed in both material samples; however, the interbead void defects were magnified due to steered fibres. This was particularly marked in the case of the cGF/PA samples, where the fibre bent because of their lower stiffness.

Under quasi-static conditions, the cCF/PA profiles performance was better than the cGF/PAs. The *SEA* of the cCF/PA specimen was 30% higher than the cGF/PA for radial loading, and almost the same for axial loading. Nevertheless, a more ductile behaviour of the cGF/PA profile was observed due to its greater toughness. As regards the impact tests, the *SEA* values obtained under radial loading for the cGF/PA profiles were higher than the quasi-static test, and higher than the values observed for the cCF/PA (85% and 42% respectively). The impact response of the cGF/PA profile was enhanced as the material presented a strain-rate dependency, whereas the cCF/PA exhibited a marked decrease in properties.

Despite the specific microstructural differences generated during 3D printing, the nature of the constituents (fibre and matrix) controlled the differences between the crush behaviour of both profiles. Difference between the fracture mechanisms and the strain-rate dependency exhibited by the cGF/PA samples could be explained through the nature (semicrystalline) of the cGF/PA matrix. Firstly, the lower interface bonding of the cGF/PA samples promoted the energy absorption through a stable growth of the delaminated zone and enhanced the slippage between layers. Moreover, the increase of the temperature of the cGF/PA samples above its T_g during impact event provoked a softer response of the profile, added to the strain-hardening response exhibited by the glass fibres, enables higher energy dissipation and better performance under impact crushing.

Although, the axial *SEA* values for cCF/PA and cGF/PA profiles were lower than those obtained for conventional manufactured profiles, the obtained radial *SEA* values for steered continuous carbon or glass fibres were at least four times higher than the best values found in the literature. Thus, concentrically printed reinforcements could be employed as local strengthening of radially loaded hollow profiles.

Authorship contribution statement

U. Morales: Methodology, Investigation, Visualization, Writing - Original Draft

A. Esnaola: Methodology, Investigation, Writing - Review & Editing, Project administration

M. Iragi: Investigation, Visualization

L. Aretxabaleta: Investigation, Validation, Writing - Review & Editing

J. Aurrekoetxea: Conceptualization, Validation, Writing - Original Draft, Funding acquisition

Declaration of Competing Interest

The authors declare that they have no known competing financial interests or personal relationships that could have appeared to influence the work reported in this paper.

Acknowledgments

Authors thank the Ministry of Science and Innovation, Spain through project ADDICOMP (grant RTI2018-094435-B-C33), the Basque Government (IT883-16) and the Gipuzkoako Foru Aldundia (RF0340/2019(ES)) for the provided financial support. Authors thank also K. Larranaga from Edertek for his support with the Dynatup 8120.

References

[1] Kaluza A, Kleemann S, Fröhlich T, Herrmann C, Vietor T. Concurrent Design & Life Cycle Engineering in Automotive Lightweight Component Development. Procedia CIRP, 2017. https://doi.org/10.1016/j.procir.2017.03.293.

[2] Mayyas A, Qattawi A, Omar M, Shan D. Design for sustainability in automotive industry: A comprehensive review. Renew Sustain Energy Rev 2012. https://doi.org/10.1016/j.rser.2012.01.012.

[3] González C, Vilatela JJ, Molina-Aldareguía JM, Lopes CS, LLorca J. Structural composites for multifunctional applications: Current challenges and future trends. Prog Mater Sci 2017;89:194–251. https://doi.org/10.1016/j.pmatsci.2017.04.005.

[4] Hull D. A unified approach to progressive crushing of fibre-reinforced composite tubes. Compos Sci Technol 1991;40. https://doi.org/10.1016/0266-3538(91)90031-J.

[5] Mamalis AG, Manolakos DE, Demosthenous GA, Ioannidis MB. Crash worthiness of composite thin-walled structural components. 1998. https://doi.org/10.1201/9781315140452.

[6] Palanivelu S, Paepegem W Van, Degrieck J, Vantomme J, Kakogiannis D, Ackeren J Van, et al. Crushing and energy absorption performance of different geometrical shapes of small-scale glass/polyester composite tubes under quasi-static loading conditions. Compos Struct 2011;93:992–1007. https://doi.org/10.1016/j.compstruct.2010.06.021.

[7] Saenz-Dominguez I, Tena I, Esnaola A, Sarrionandia M, Torre J, Aurrekoetxea J. Design and characterisation of cellular composite structures for automotive crash-boxes manufactured by out of die ultraviolet cured pultrusion. Compos Part B Eng 2019;160:217–24. https://doi.org/10.1016/j.compositesb.2018.10.046.

[8] Tena I, Esnaola A, Sarrionandia M, Ulacia I, Torre J, Aurrekoetxea J. Out of die ultraviolet cured pultrusion for automotive crash structures. Compos Part B Eng 2015;79:209–16. https://doi.org/10.1016/j.compositesb.2015.04.044.

[9] Esnaola A, Tena I, Aurrekoetxea J, Gallego I, Ulacia I. Effect of fibre volume fraction on energy absorption capabilities of E-glass/polyester automotive crash structures. Compos Part B Eng 2016;85:1–7. https://doi.org/10.1016/j.compositesb.2015.09.007.

[10] Belingardi G, Beyene AT, Koricho EG. Geometrical optimization of bumper beam profile made of pultruded composite by numerical simulation. Compos Struct 2013;102:217–25. https://doi.org/10.1016/j.compstruct.2013.02.013.

[11] Abdewi EF, Sulaiman S, Hamouda AMS, Mahdi E. Quasi-static axial and lateral crushing of radial corrugated composite tubes. Thin-Walled Struct 2008;46:320–32. https://doi.org/10.1016/j.tws.2007.07.018.

[12] Mamalis AG, Manolakos DE, Ioannidis MB, Papapostolou DP. On the response of thin-walled CFRP composite tubular components subjected to static and dynamic axial compressive loading: Experimental. Compos Struct 2005;69:407–20. https://doi.org/10.1016/j.compstruct.2004.07.021.

[13] Hamada H, Coppola JC, Hull D, Maekawa Z, Sato H. Comparison of energy absorption of carbon/epoxy and carbon/PEEK composite tubes. Composites 1992;23:245–52. https://doi.org/10.1016/0010-4361(92)90184-V.

[14] Frketic J, Dickens T, Ramakrishnan S. Automated manufacturing and processing of fiber-reinforced polymer (FRP) composites: An additive review of contemporary and modern techniques for advanced materials manufacturing. Addit Manuf 2017;14:69–86. https://doi.org/10.1016/j.addma.2017.01.003.

[15] Wang X, Jiang M, Zhou Z, Gou J, Hui D. 3D printing of polymer matrix composites: A review and prospective. Compos Part B Eng 2017;110:442–58. https://doi.org/10.1016/j.compositesb.2016.11.034.

[16] Parandoush P, Lin D. A review on additive manufacturing of polymer-fiber composites. Compos Struct 2017;182:36–53. https://doi.org/10.1016/j.compstruct.2017.08.088.

[17] Goh GD, Yap YL, Agarwala S, Yeong WY. Recent Progress in Additive Manufacturing of Fiber Reinforced Polymer Composite. Adv Mater Technol 2019. https://doi.org/10.1002/admt.201800271.

[18] Mark GT, Gozdz AS. Apparatus for fiber reinforced additive manufacturing, 2014, US 2014/9630328 A1.

[19] Dickson AN, Barry JN, McDonnell KA, Dowling DP. Fabrication of continuous carbon, glass and Kevlar fibre reinforced polymer composites using additive manufacturing. Addit Manuf 2017. https://doi.org/10.1016/j.addma.2017.06.004.

[20] Chabaud G, Castro M, Denoual C, Le Duigou A. Hygromechanical properties of 3D printed continuous carbon and glass fibre reinforced polyamide composite for outdoor structural applications. Addit Manuf 2019. https://doi.org/10.1016/j.addma.2019.01.005.

[21] Al Abadi H, Thai HT, Paton-Cole V, Patel VI. Elastic properties of 3D printed fibre-reinforced structures. Compos Struct 2018. https://doi.org/10.1016/j.compstruct.2018.03.051.

[22] Liu T, Tian X, Zhang M, Abliz D, Li D, Ziegmann G. Interfacial performance and fracture patterns of 3D printed continuous carbon fiber with sizing reinforced PA6 composites. Compos Part A Appl Sci Manuf 2018;114:368–76. https://doi.org/10.1016/j.compositesa.2018.09.001.

[23] Goh GD, Dikshit V, Nagalingam AP, Goh GL, Agarwala S, Sing SL, et al. Characterization of mechanical properties and fracture mode of additively manufactured carbon fiber and glass fiber reinforced thermoplastics. Mater Des 2018;137:79–89.https://doi.org/10.1016/j.matdes.2017.10.021.

[24] Justo J, Távara L, García-Guzmán L, París F. Characterization of 3D printed long fibre reinforced composites. Compos Struct 2018;185:537–48. https://doi.org/10.1016/j.compstruct.2017.11.052.

[25] Caminero MA, Chacón JM, García-Moreno I, Reverte JM. Interlaminar bonding performance of 3D printed continuous fibre reinforced thermoplastic composites using fused deposition modelling. Polym Test 2018;68:415–23. https://doi.org/10.1016/j.polymertesting.2018.04.038.

[26] Yogeshvaran RN, Liu BG, Farukh F, Kandan K. Out-of-Plane Compressive Response of Additively Manufactured Cross-Ply Composites. J Mech 2020;36. https://doi.org/10.1017/jmech.2019.59

[27] Araya-Calvo M, López-Gómez I, Chamberlain-Simon N, León-Salazar JL, Guillén-Girón T, Corrales-Cordero JS, et al. Evaluation of compressive and flexural properties of continuous fiber fabrication additive manufacturing technology. Addit Manuf 2018;22:157–64. https://doi.org/10.1016/j.addma.2018.05.007.

[28] Iragi M, Pascual-González C, Esnaola A, Lopes CS, Aretxabaleta L. Ply and interlaminar behaviours of 3D printed continuous carbon fibre-reinforced thermoplastic laminates; effects of processing conditions and microstructure. Addit Manuf 2019;30. https://doi.org/10.1016/j.addma.2019.100884.

[29] Chacón JM, Caminero MA, Núñez PJ, García-Plaza E, García-Moreno I, Reverte JM. Additive manufacturing of continuous fibre reinforced thermoplastic composites using fused deposition modelling: Effect of process parameters on mechanical properties. Compos Sci Technol 2019. https://doi.org/10.1016/j.compscitech.2019.107688.

[30] Blok LG, Longana ML, Yu H, Woods BKS. An investigation into 3D printing of fibre reinforced thermoplastic composites. Addit Manuf 2018;22:176–86. https://doi.org/10.1016/j.addma.2018.04.039.

[31] Pascual-González C, Iragi M, Fernández A, Fernández-Blázquez JP, Aretxabaleta L, Lopes CS. An approach to analyse the factors behind the micromechanical response of 3D-printed composites. Compos Part B Eng 2020;186. https://doi.org/10.1016/j.compositesb.2020.107820.

[32] Caminero MA, Chacón JM, García-Moreno I, Rodríguez GP. Impact damage resistance of 3D printed continuous fibre reinforced thermoplastic composites using fused deposition modelling. Compos Part B Eng 2018;148:93–103. https://doi.org/10.1016/j.compositesb.2018.04.054.

[33] Harding J, Welsh LM. A tensile testing technique for fibre-reinforced composites at impact rates of strain. J Mater Sci 1983;18:1810–26. https://doi.org/10.1007/BF00542078.

[34] Farley GL. The Effects of Crushing Speed on the Energy-Absorption Capability of Composite Tubes. J Compos Mater 1991;25. https://doi.org/10.1177/002199839102501004.

[35] Farley GL, Jones RM. Crushing Characteristics of Continuous Fiber-Reinforced Composite Tubes. J Compos Mater 1992;26:37–50. https://doi.org/10.1177/002199839202600103.

[36] Shah SZH, Karuppanan S, Megat-Yusoff PSM, Sajid Z. Impact resistance and damage tolerance of fiber reinforced composites: A review. Compos Struct 2019;217. https://doi.org/10.1016/j.compstruct.2019.03.021.

[37] Vieille B, Casado VM, Bouvet C. About the impact behavior of woven-ply carbon fiber-reinforced thermoplastic- and thermosetting-composites: A comparative study. Compos Struct 2013;101. https://doi.org/10.1016/j.compstruct.2013.01.025.

[38] Siviour CR, Jordan JL. High Strain Rate Mechanics of Polymers: A Review. J Dyn Behav Mater 2016. https://doi.org/10.1007/s40870-016-0052-8.

[39] Arao Y, Taniguchi N, Nishiwaki T, Hirayama N, Kawada H. Strain-rate dependence of the tensile strength of glass fibers. J Mater Sci 2012;47. https://doi.org/10.1007/s10853-012-6360-z.

[40] van de Werken N, Hurley J, Khanbolouki P, Sarvestani AN, Tamijani AY, Tehrani M. Design considerations and modeling of fiber reinforced 3D printed parts. Compos Part B Eng 2019. https://doi.org/10.1016/j.compositesb.2018.12.094.

[41] Matsuzaki R, Nakamura T, Sugiyama K, Ueda M, Todoroki A, Hirano Y, et al. Effects of Set Curvature and Fiber Bundle Size on the Printed Radius of Curvature by a Continuous Carbon Fiber Composite 3D Printer. Addit Manuf 2018;24:93–102. https://doi.org/10.1016/j.addma.2018.09.019.

[42] Shiratori H, Todoroki A, Ueda M, Matsuzaki R, Hirano Y. Mechanism of folding a fiber bundle in the curved section of 3D printed carbon fiber reinforced plastics. Adv Compos Mater 2020. https://doi.org/10.1080/09243046.2019.1682794.

Vitae

Mechanical Engineer graduated from UPV/EHU Engineering Technical School (University of Basque Country) in 2006. He has been working during ten years in TECNALIA RESEARCH AND INNOVATION (Basque Country R&D centre). Since 2017, he is a PhD student at the research group of Polymer and Composites Technology at Mondragon Unibersity. His reserach is focused on Design and Optimization of 3D printed composite structures, developing lightweighting solutions and impact loading applications. He actually is involved in different fundamental research projects such as European projects or industrial transfer projects oriented to the automotive industry and mechanical engineering equipments.

Table 1. Transverse section's geometrical properties.

Profile	**Area** (mm^2)	I_{yy} (mm^4)
Fold	333.6	45656

Table 2. Extrusion and filling parameters of the printing process.

Extrusion parameter	**Value**		**Value**		**Filling parameter**	**Value**
Material	Onyx®	cCF/PA	Onyx®	cGF/PA	Filling pattern	Concentric
Layer thickness (mm)	0.125		0.1		Number of floor/roof layer	2
Nozzle diameter (mm)	0.4	0.9	0.4	0.9	Number of wall contours	1
Temperature (ºC)	273	252	273	252	Concentric Fibre Rings	2
Printing speed (mm/s)	15		10		Fibre Angles - Walls to Reinforce	All walls

Table 3. Static compression test results.

Test specimen	**Crush Stroke** l (mm)	**Mean Load** P_{mean} (kN)	**Max Load** P_{max} (kN)	**Energy Abs.** E_{abs} (J)	**Specific Energy** *SEA* (kJ/kg)	**Failure Mode** (-)
CSA						
- Peak load	12.3	12.0 (±0.2)	22.2 (±0.7)	169.0 (±5.9)	30.1 (±0.5)	Stable
- Plateau	30.0		10.4 (±2.3)	352.0 (±10.1)		
- 60% stroke	36.0		14.7 (±1.3)	433.7 (±6.9)		
CSR						
- 1º Peak load	6.6	6.2 (±0.4)	7.0 (±0.9)	34.9 (±1.6)	9.0 (±0.6)	Stable
- Plateau	14.4		4.0 (±1.3)	62.9 (±3.2)		
- 2º peak load	19.0		12.8 (±1.7)	109.2 (±8.8)		
- 60% stroke	21.0		12.6 (±2.4)	127.0 (±8.3)		
GSA						
- Peak load	8.3	15.7 (±1.1)	24.9 (±1.8)	139.7 (±24.8)	31.4 (±2.1)	Stable
- Plateau	24.0		14.0 (±0.4)	367.3 (±23.9)		
- 60% stroke	36.0		23.1 (±1.3)	557.0 (±36.0)		
GSR						
- 1º Peak load	4.6	5.9 (±1.9)	5.0 (±1.6)	14.3 (±4.4)	6.9 (±2.2)	Stable
- Plateau	14.4		5.4 (±3.0)	66.9 (±23.8)		
- 2º peak load	17.6		8.9 (±4.3)	90.7 (±35.5)		
- 60% stroke	21.0		10.4 (±3.5)	123.7 (±39.3)		

Table 4. Impact test results.

Test specimen	**Crush Stroke** l (mm)	**Mean Load** P_{mean} (kN)	**Max Load** P_{max} (kN)	**Abs. Energy** E_{abs} (J)	**Specific Energy** SEA (kJ/kg)	**Failure Mode** (-)
CDA						
- 60% stroke	36	6.6 (±0.4)	19.7 (±0.8)	236.8 (±13.7)	16.4 (±0.9)	Stable
CDR						
- 60% stroke	21	3.0 (±0.4)	7.4 (±1.1)	63.7 (±8.7)	4.4 (±0.6)	Stable
GDA						
- 60% stroke	36	10.0 (±0.1)	19.0 (±0.3)	359.4 (±2.4)	20.0 (±0.1)	Stable
GDR						
- 60% stroke	21	11.0 (±0.2)	19.0 (±1.6)	231.2 (±4.5)	12.8 (±0.3)	Stable

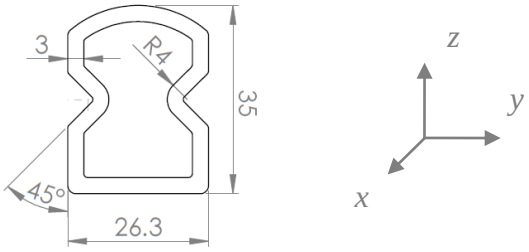

a)

Figure 1. Profile geometries; Fold [10].

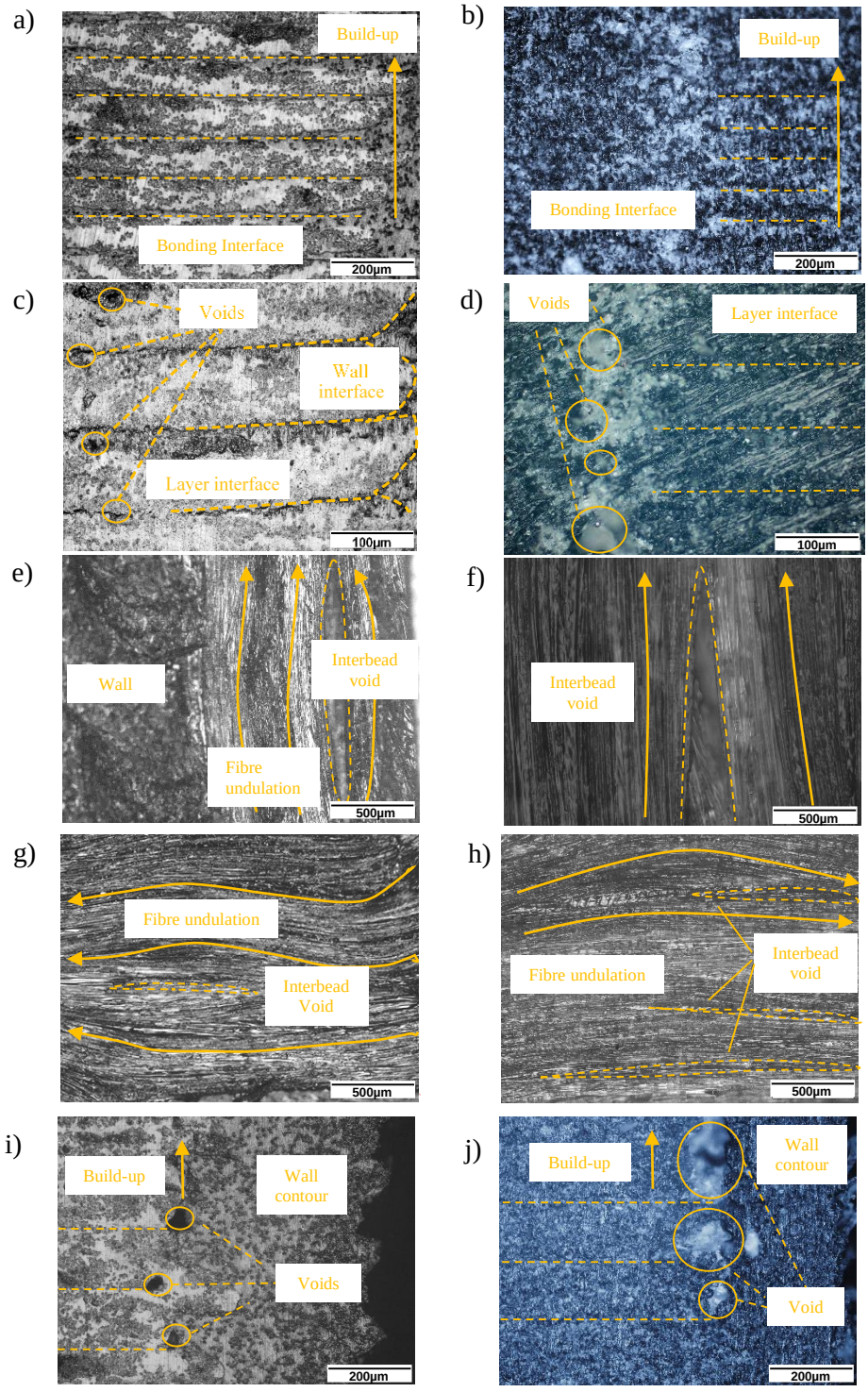

Figure 2. Printing quality and interface aspect of materials as printed.
Bonding interface and built-up aspect: a) cCF/PA and b) cGF/PA samples.
Interlayer voids: c) cCF/PA and d) cGF/PA samples.
Interbead voids: e) cCF/PA and f) cGF/PA samples.
Fibre undulation including straight printing paths: g) cCF/PA and h) cGF/PA samples.
Onyx wall contour and interface with inner fibre beads: i) cCF/PA and j) cGF/PA samples.

Color should be used for Figure 2 in print

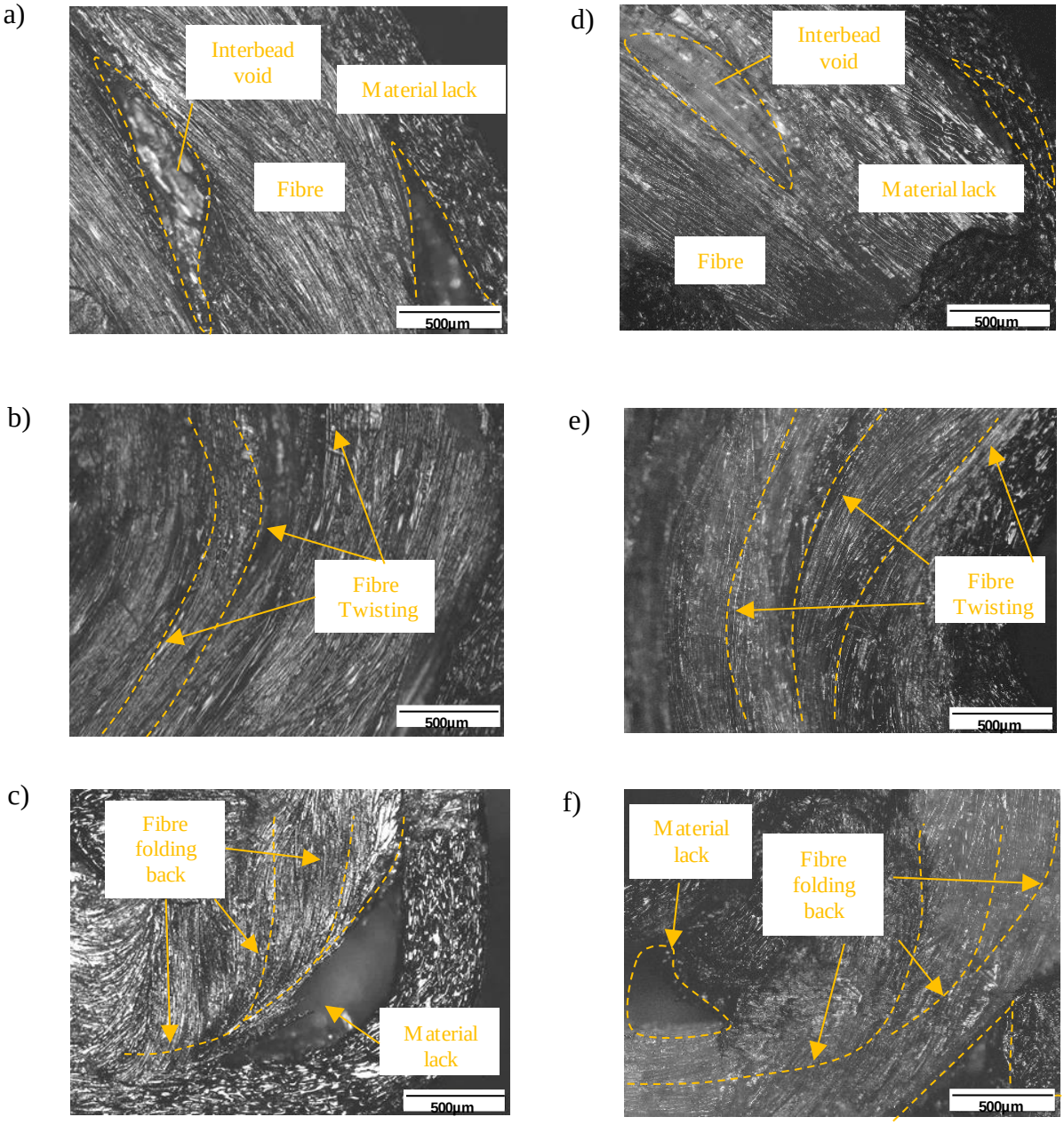

Figure 3. Defects of fibre-placement. cCF/PA sample: a) Interbead void, b) Fibre twisting, and c) Folding back. cGF/PA sample: d) Interbead void, e) Fibre twisting and f) Folding back.

Color should be used for figure 3 in print

a)

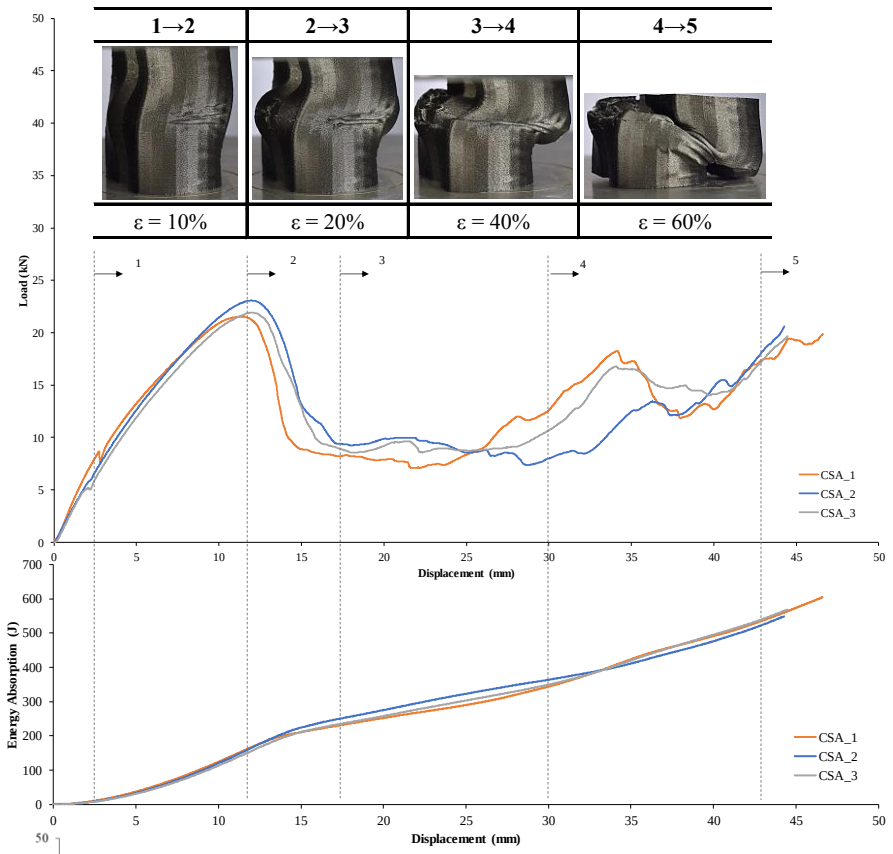

b)

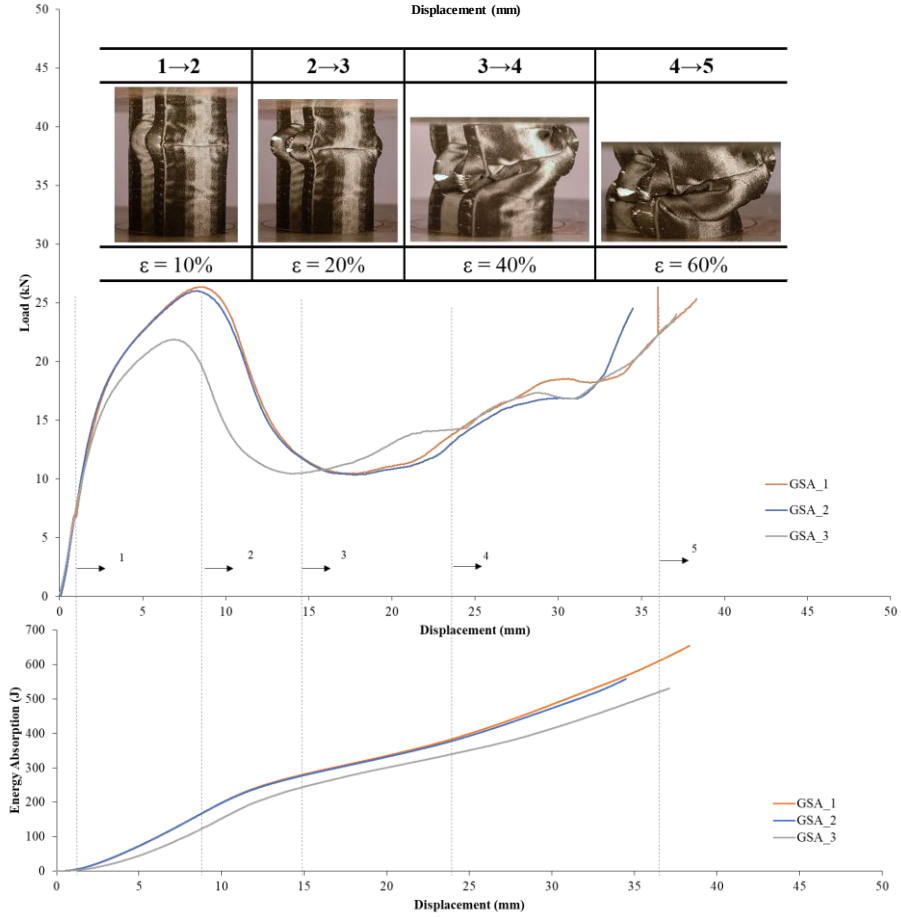

Figure 4. Axial crush curves and patterns a) for cCF/PA and b) for cGF/PA profiles.
Color should be used for Figure 4 in print

a)

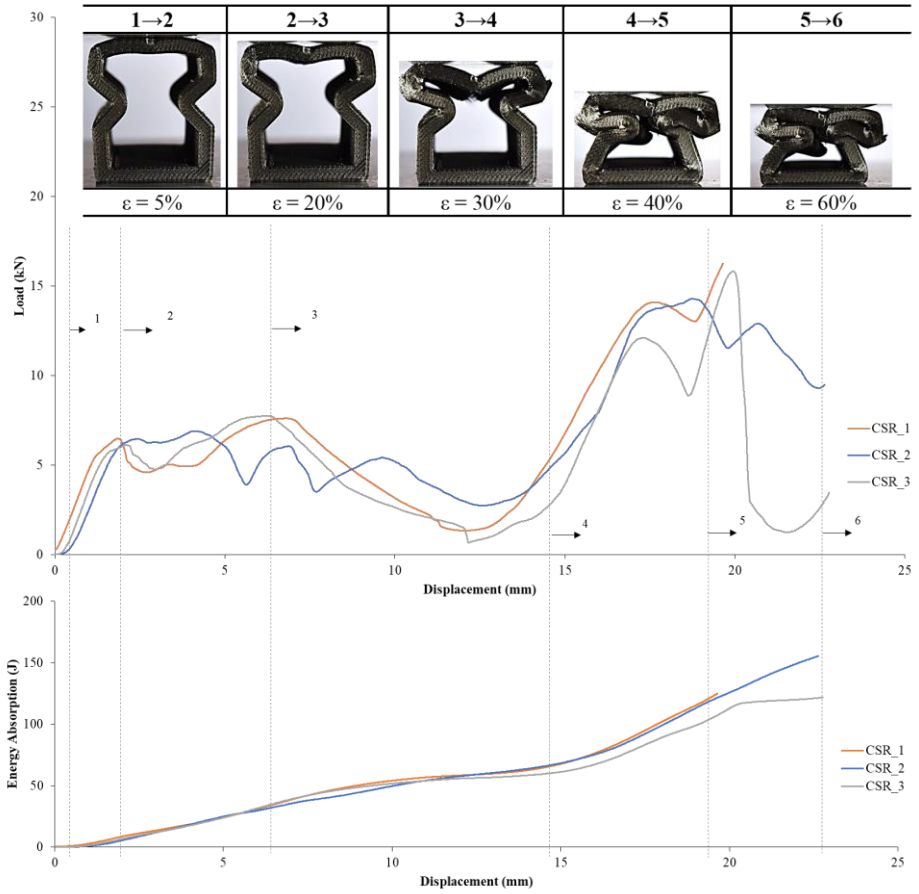

b)

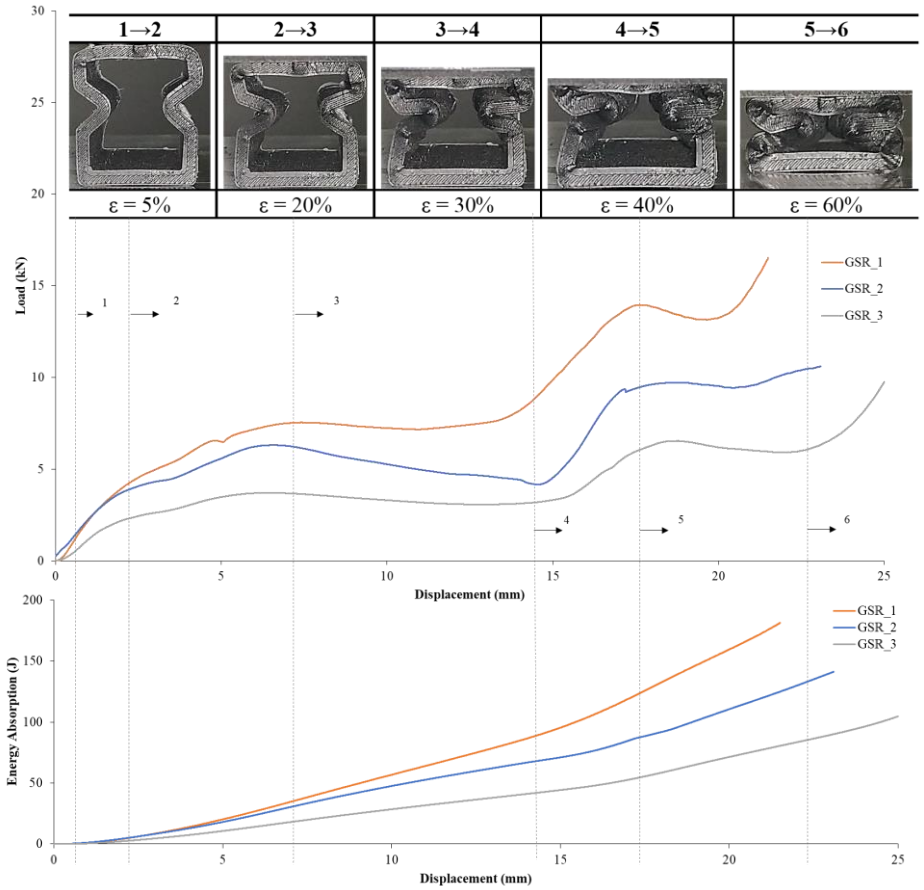

Figure 5. Radial crush curves and patterns a) for cCF/PA and b) for cGF/PA profiles.
Color should be used for Figure 5 in print

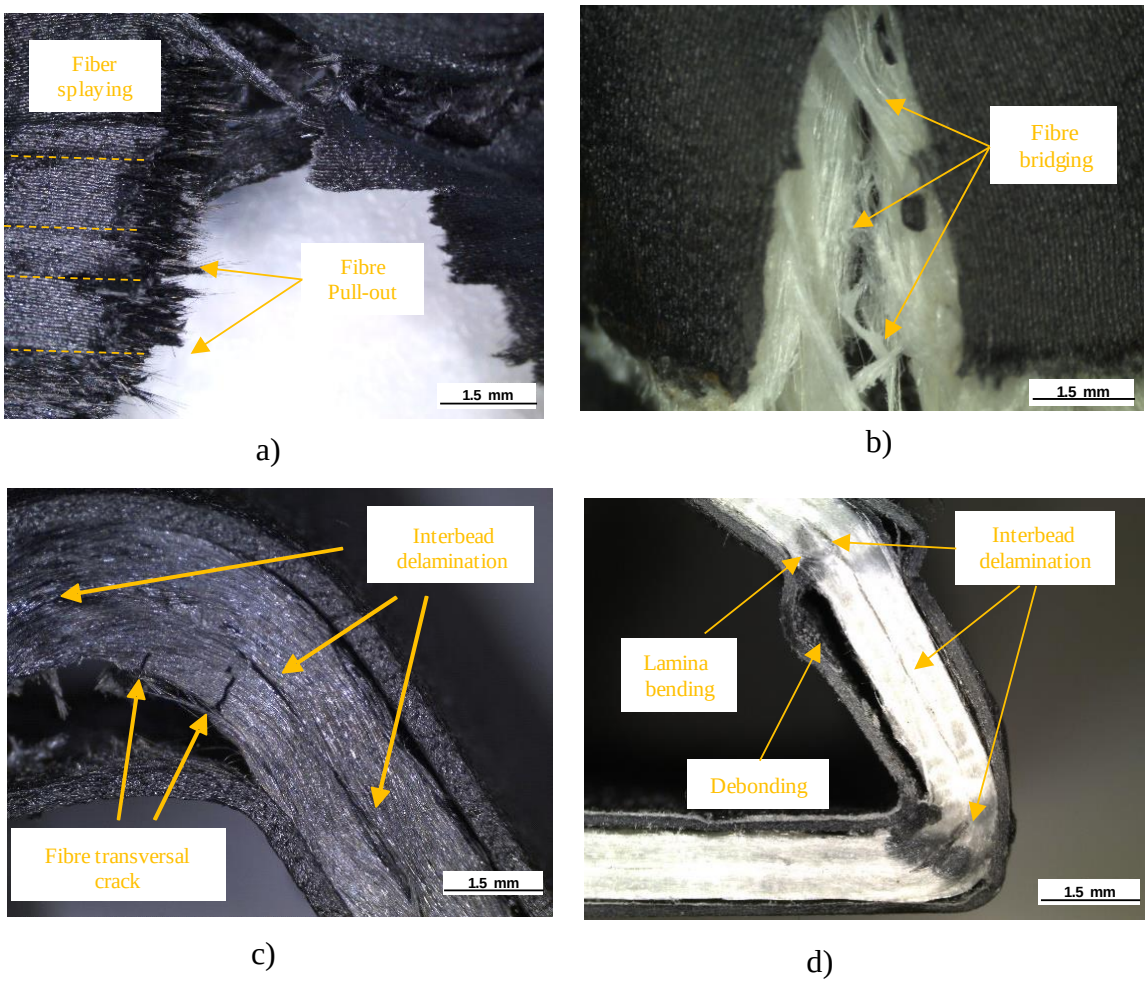

Figure 6. Fracture surface and failure mode. a) Fibre splaying and fibre pull-out on CSA, b) Fibre bridging on GSA, c) Fibre transverse crack and interbead delamination on CSR and d) Debonding, lamina bending and interbead delamination on GSR.

Color should be used for Figure 6 in print

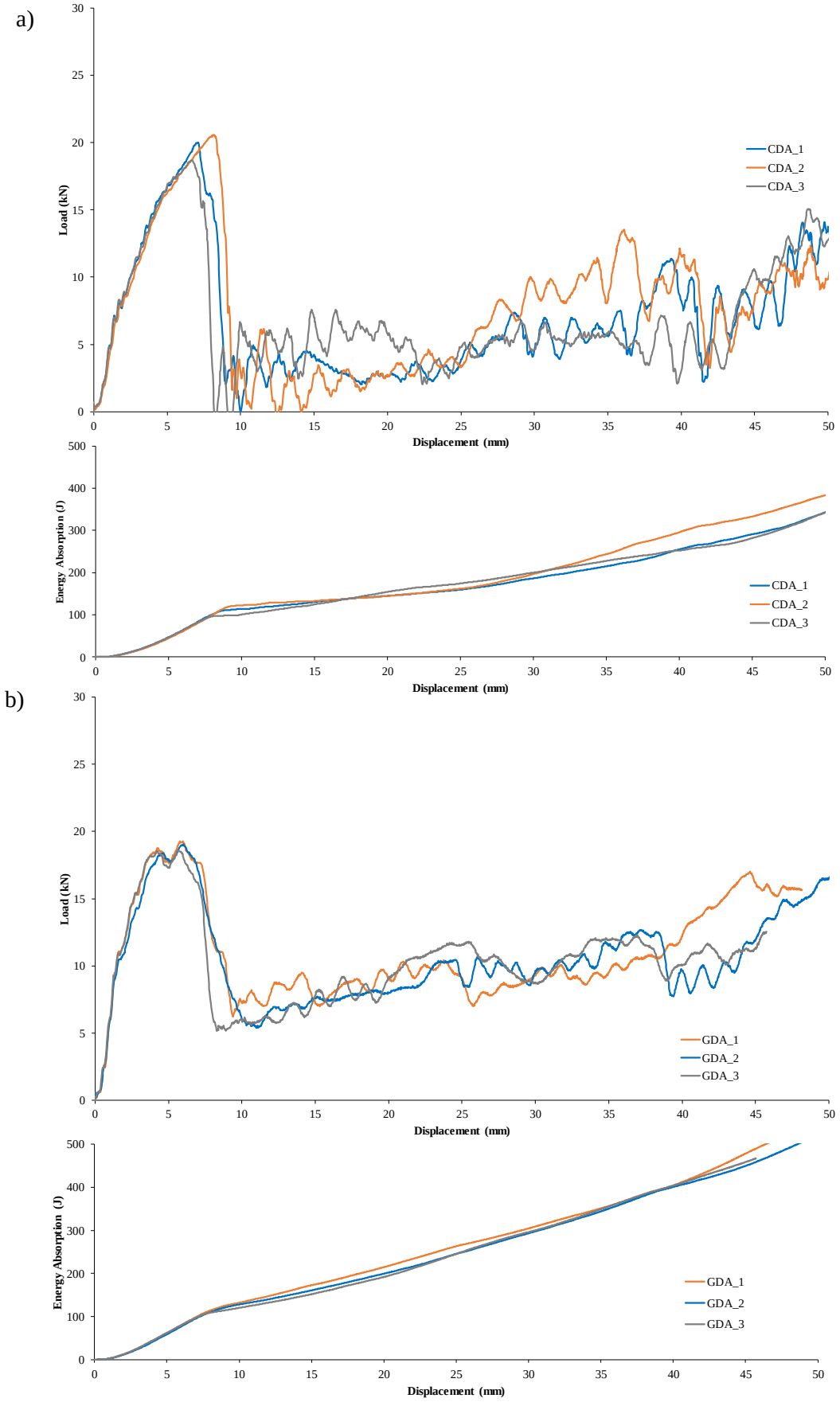

Figure 7. Axial impact curves a) for cCF/PA and b) for cGF/PA profiles.
Color should be used for figure 7 in print

a)

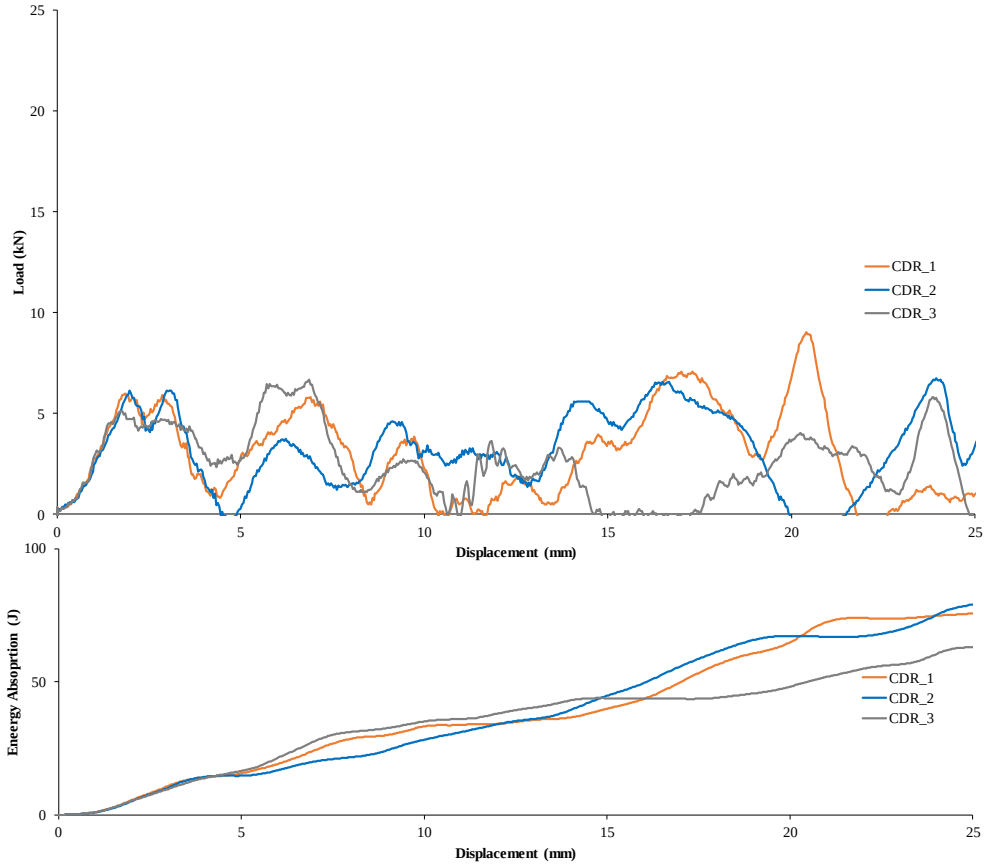

b)

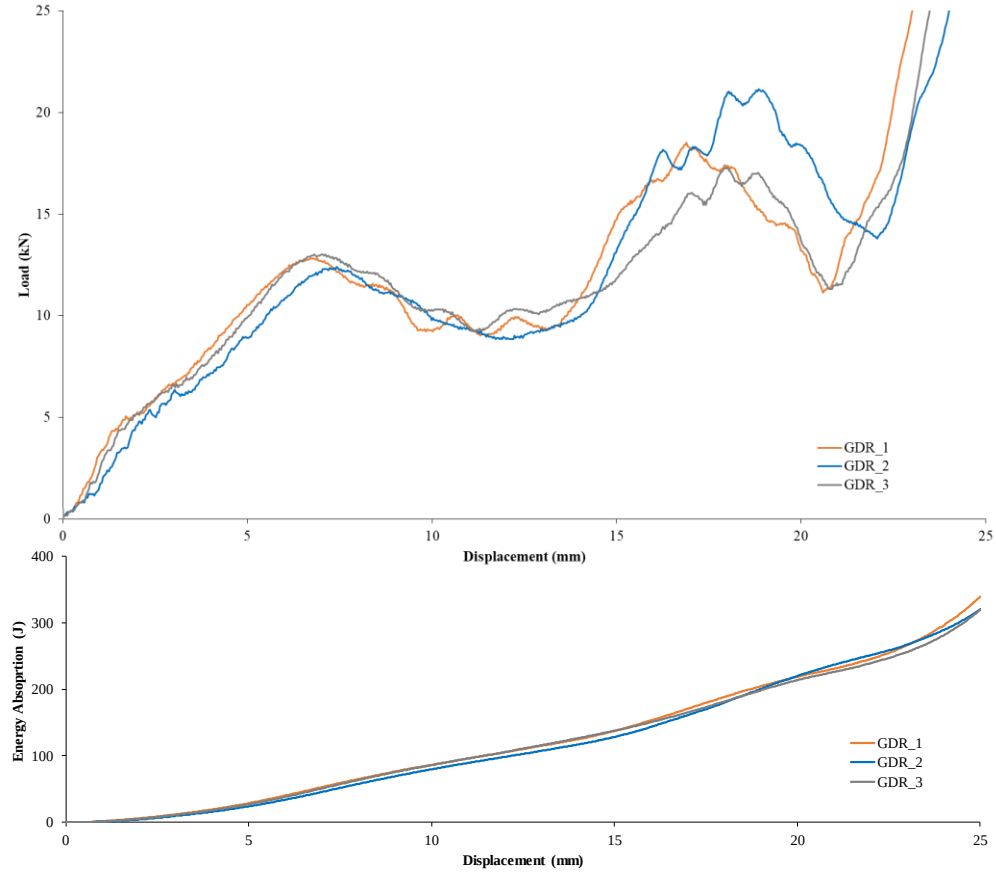

Figure 8. Radial impact curves a) for cCF/PA and b) for cGF/PA profiles.
Color should be used for figure 8 in print

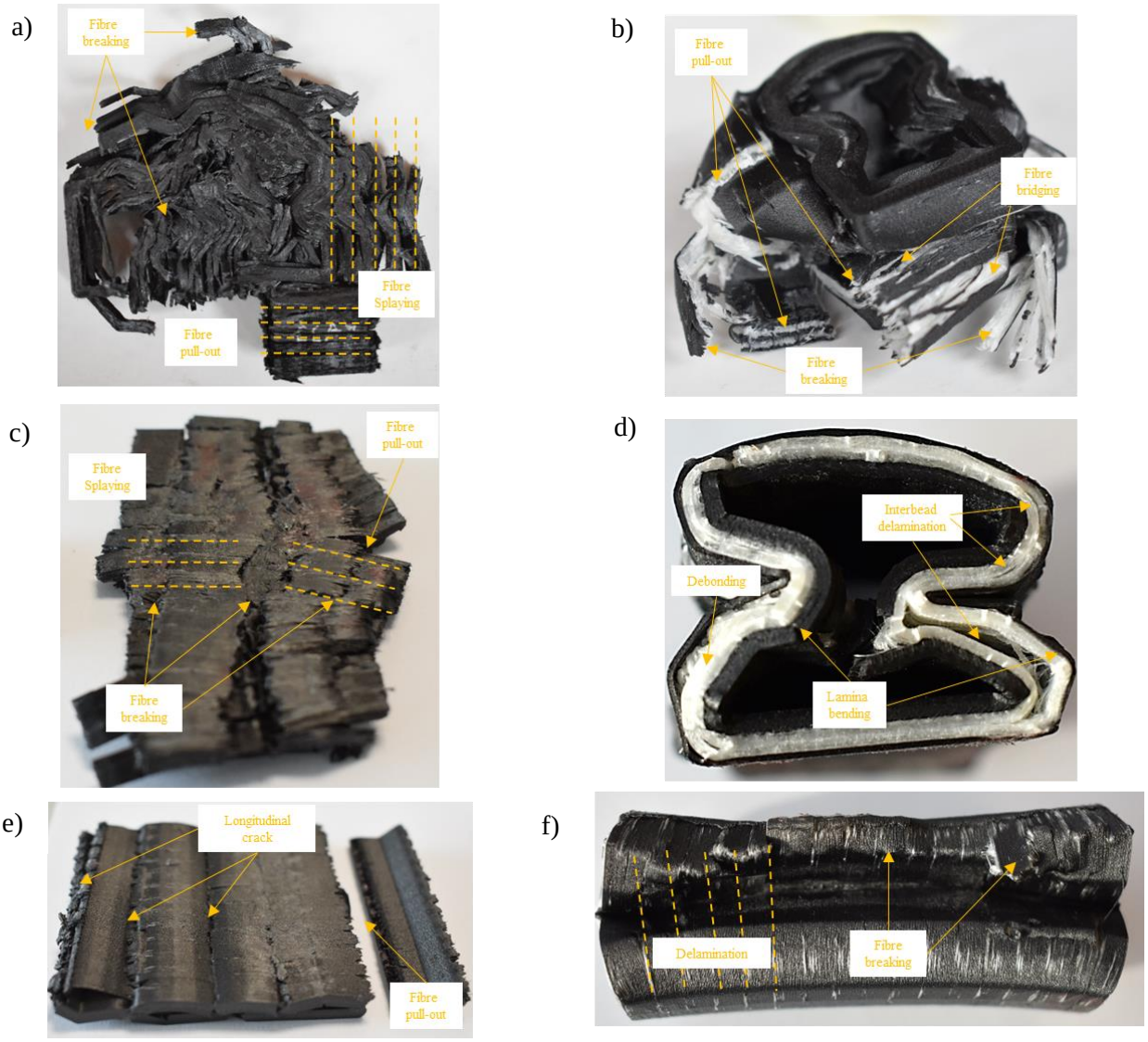

Figure 9. Post-impacted profiles. a) Fibre splaying and breaking on CDA, b) Fibre bridging and breaking on GDA, c) Fibre breaking and pull-out on CDR, d) Interbead delamination and lamina bending on GDR, e) Longitunal crack on CDR f) Interlayer delamination and fibre breaking on GDR.

Color should be used for figure 9 in print